HHS Public Access

Author manuscript

Sci Immunol. Author manuscript; available in PMC 2020 August 28.

Published in final edited form as:

Sci Immunol. 2020 February 28; 5(44): . doi:10.1126/sciimmunol.aax1036.

PAX1 is essential for development and function of the human thymus

Yasuhiro Yamazaki[1], **Raul Urrutia**[2], **Luis M. Franco**[3], **Silvia Giliani**[4,5], **Kejian Zhang**[6,7], **Anas M. Alazami**[8,9], **A. Kerry Dobbs**[1], **Stefania Masneri**[4,5], **Avni Joshi**[10], **Francisco Otaizo-Carrasquero**[11], **Timothy G. Myers**[11], **Sundar Ganesan**[12], **Maria Pia Bondioni**[13], **Mai Lan Ho**[14], **Catherine Marks**[14], **Huda Alajlan**[8], **Reem W Mohammed**[15], **Fanggeng Zou**[7,16], **C. Alexander Valencia**[7,17,29,30], **Alexandra H. Filipovich**[18], **Fabio Facchetti**[4], **Bertrand Boisson**[19,20,21], **Chiara Azzari**[22,23], **Bander K. Al-Saud**[15,24], **Hamoud Al-Mousa**[15,24], **Jean Laurent Casanova**[19,20,21,25,26], **Roshini S. Abraham**[27,28], **Luigi D. Notarangelo**[1,*]

[1]Laboratory of Clinical Immunology and Microbiology, NIAID, NIH, Bethesda, MD 20892, USA

[2]Human and Molecular Genetics Center, Medical College Wisconsin, Milwaukee, MI, USA

[3]Systemic Autoimmunity Branch, NIAMS, NIH, Bethesda, MD 20892, USA

[4]Department of Molecular and Translational Medicine, University of Brescia, Brescia, Italy

[5]Cytogenetic and Medical Genetics Unit, “A. Nocivelli” Institute for Molecular Medicine, Spedali Civili Hospital, Brescia, Italy

[6]Coyote Bioscience USA Inc., San Jose, CA 95138, USA

[7]Division of Human Genetics, Cincinnati Children’s Hospital Medical Center, University of Cincinnati, College of Medicine, Cincinnati, OH 45229, USA

[8]Department of Genetics, King Faisal Specialist Hospital and Research Centre, Riyadh 11211, Saudi Arabia

[9]Saudi Human Genome Program, King Abdulaziz City for Science and Technology, Riyadh, Saudi Arabia

[10]Division of Pediatric Allergy and Immunology, Mayo Clinic Children’s Center, Rochester, MN, USA

[*]Corresponding author. luigi.notarangelo2@nih.gov.

Author contributions: YY performed experiments and wrote the manuscript; RU performed structural modeling and molecular dynamics simulation studies; LF supervised analysis of RNAseq and GSEA data; FO-C and TM assisted with RNAseq studies; SG and SM performed Sanger sequencing and Western blot analysis, and analyzed WES data; KZ, AMA, HA, FZ, CAV and BB performed and analyzed WES; AKD generated iPSCs; AJ, RWM, AHF, CA, BKA-S, and H-AM provided clinical care and description of the patients; FF performed lymph node pathology; MPB, MLH and CM performed and interpreted imaging studies; JLC and RSA contributed to supervision of the project and to writing of the manuscript; LDN was responsible for the entire research project and wrote the manuscript.

Competing interests: The authors declare no competing interests.

Data and materials availability: Fibroblast and iPSC lines from P1 and P4 are available upon request but are contingent upon approval of Material and Transfer Agreement by the NIAID, NIH. WES data have been uploaded to the NCBI SRA Submission Portal, with the following ID: PRJNA601119. The RNA-sequencing data set for this study has been uploaded to the National Center for Biotechnology Information (NCBI) Gene Expression Omnibus (GEO), under accession no. GSE138784. The GEO accession includes links to the NCBI Sequence Read Archive (SRA) database, from which the raw data will be accessible in FASTQ format, under accession no. SRP225226.

[11]Genomic Technologies Section, NIAID, NIH, Bethesda, MD 20892, USA

[12]Research Technologies Branch, DIR, NIAID, NIH, Bethesda, MD 20892, USA

[13]Department of Medical and Surgical Specialties, Radiological Sciences and Public Health, University of Brescia, Brescia, Italy

[14]Department of Radiology, Mayo Clinic, Rochester, MN, USA

[15]Alfaisal University, Riyadh, Saudi Arabia

[16]GeneDx Inc., Gaithersburg, MD 20877, USA

[17]PerkinElmer Genomics, Pittsburgh, PA 15275, USA

[18]Cancer and Blood Institute, Cincinnati Children's Hospital Medical Center, University of Cincinnati, College of Medicine, Cincinnati, OH 45229, USA

[19]St. Giles Laboratory of Human Genetics of Infectious Diseases, Rockefeller Branch, Rockefeller University, New York, NY 10065, USA

[20]Laboratory of Human Genetics of Infectious Diseases, Necker Branch INSERM, Necker Hospital for Sick Children, Paris, France

[21]Paris Descartes University, Imagine Institute, Paris, France

[22]Pediatric Immunology, Department of Health Sciences, University of Florence, Florence, Italy

[23]Meyer Children's Hospital, Florence, Italy

[24]Department of Pediatrics, Allergy and Immunology Section, King Faisal Specialist Hospital and Research Centre, Riyadh 11211, Saudi Arabia

[25]Pediatrics Hematology-Immunology Unit, Necker Hospital for Sick Children, Paris, France

[26]Howard Hughes Medical Institute, New York, NY 10065, USA

[27]Department of Laboratory Medicine and Pathology, Mayo Clinic, Rochester, MN 55905, USA

[28]Department of Pathology and Laboratory Medicine, Nationwide Children's Hospital, Columbus, OH 43205, USA

[29]Department of Geriatrics, West China Hospital, Sichuan University, Chengdu, China

[30]Aperiomics, Inc., Sterling, VA 20166, USA

Abstract

We investigated the molecular and cellular basis of severe combined immunodeficiency (SCID) in six patients with otofaciocervical syndrome type 2 who failed to attain T cell reconstitution after allogeneic hematopoietic stem cell transplantation, despite successful engraftment in three of them. We identified rare bi-allelic *PAX1* rare variants in all patients. We demonstrated that these mutant PAX1 proteins have an altered conformation and flexibility of the paired box domain and reduced transcriptional activity. We generated patient-derived induced pluripotent stem cells and differentiated them into thymic epithelial progenitor cells, and found that they have an altered transcriptional profile, including for genes involved in the development of the thymus and other

tissues derived from pharyngeal pouches. These results identify bi-allelic, loss-of-function *PAX1* mutations as the cause of a syndromic form of SCID due to altered thymus development.

One Sentence Summary

PAX1 deficiency causes a syndromic form of SCID by altering differentiation of thymic epithelial cells and other pharyngeal pouch tissues.

Introduction

Severe combined immunodeficiency (SCID) is a heterogeneous group of genetic diseases characterized by severe T cell lymphopenia, causing increased susceptibility to viral, bacterial, and fungal infections since early in life (1). Most forms of SCID are due to genetic defects that are intrinsic to hematopoietic cells, and can be successfully treated by allogeneic hematopoietic stem cell transplantation (HSCT). However, SCID may also be caused by genetic abnormalities that are intrinsic to thymic epithelium development and function; in such cases, thymus transplantation, but not HCT, is required to cure the disease. Only a few genetic abnormalities, including complete DiGeorge syndrome, and pathogenic variants affecting *FOXN1* or *CHD7,* are known to cause SCID as a result of abnormal thymic development in humans (1).

PAX1 is a member of the paired box (PAX) family of transcription factors and plays a critical role in pattern formation during embryogenesis. It is expressed in the pharyngeal pouches that give rise to the thymus, tonsils, parathyroid glands, thyroid, and middle ear develop during human embryogenesis (2). *Pax1* deficiency in mice is characterized by anomalies of the vertebral column and variable degrees of thymic hypoplasia and thymocyte number and maturation (3–5). In humans, a homozygous pathogenic *PAX1* p.Gly166Val variant (6), and a homozygous frameshift insertion (c.1173_1174insGCCCG) (7) have been identified in patients with otofaciocervical syndrome type 2 (OTFCS2), a rare disorder characterized by facial dysmorphism, external ear anomalies with preauricular pits and hearing impairment, branchial cysts or fistulas, anomalies of the vertebrae and the shoulder girdle, and mild intellectual disability. Recently, another homozygous pathogenic *PAX1* variant (p.Cys368*) has been reported in two affected children from a consanguineous family of North African descent, who presented with OTFCS2 associated with T^- B^+ SCID (8). However, limited information was provided on the immunological phenotype of these patients, and the functional consequences of the *PAX1* variant were not investigated. Here we provide an in-depth clinical, biochemical and immunological description of multiple patients with OTFCS2 associated with SCID who carried bi-allelic deleterious *PAX1* variants. By performing transfection experiments, molecular modeling, molecular dynamics (MD) simulation, and in vitro differentiation of control- and patient-derived induced pluripotent stem cells (iPSCs) to thymic epithelial progenitor (TEP) cells, we sought to assess the effects of human PAX1 deficiency on thymus development and function.

Results

Clinical characterization of the patients

Patient 1 (P1) is a male infant born to parents whose families were from the same rural region in Germany (Fig. 1A). Bilateral microtia, malar prominence, narrow alae nasi, cupid bow lip and retrognathia were noticed at birth (Fig. S1A–B).Imaging studies demonstrated severely stenotic external auditory canal on the right side and narrow left auditory canal (Fig. S1C), congenital kyphosis at C3-C4 and L3 levels, moderate spinal canal narrowing (Fig. S1D–F) and traction on the cauda equina (Fig. S1G). Diffuse erythematous rash (Fig. S1H), lymphadenopathy, elevated serum IgE and eosinophilia were present, consistent with Omenn syndrome. On chest X-ray, the thymus shadow was not visible, and split cervical vertebral bodies, hooked distal clavicles, and a shallow dysplastic glenoid fossa were seen (Fig. S1I). His infection history during infancy included *Staphylococcus aureus* bacteremia, pneumonia, cellulitis and diarrhea due to *Clostridium difficile*.

P2 and P3 have been previously described (8) as patients V:1 and V:18, respectively, and are part of a large consanguineous family of Moroccan origin (Fig. 1A). At birth, P2 was noticed to have frontal and parietal bossing, hypertelorism, small nose with hypoplastic nasal root, low-set ears with agenesis of the left pinna and hypoplasia of the right pinna, scapular winging and bilateral cryptorchidism. Imaging studies showed impaired development of internal auditory canals bilaterally and lack of a thymic shadow. P3 manifested similar facial dysmorphisms as P2, along with left facial nerve palsy, severe dorsal and lumbar scoliosis, and deafness. Imaging studies documented lack of thymic shadow, abnormal appearance of vertebrae, clavicles and shoulder blades, narrowing of both external auditory canals (Fig. S1J), abnormalities of the middle ear, and presence of a tubular structures with features of a dental element behind the mandibular condyle (Fig. S1K–L). Subject V:3 from the same family died early in life with a history of severe infections, but no formal medical records are available.

P4 and P7 are siblings born to consanguineous parents from Saudi Arabia. P7 was noticed to have severe bilateral microtia, postauricular sinuses, and micrognathia. He suffered from chronic diarrhea, recurrent respiratory infections, exfoliative dermatitis, BCG-itis, and lymphadenopathy, and died at one year of age.

P4 is a female with a history of chronic diarrhea, recurrent respiratory infections, and poor weight gain since the age of one month. Physical examination showed small malformed ears, a skin tag on the right ear, facial asymmetry, small nose with depressed nasal bridge and small almond shaped eyes. A skeletal survey showed wedge-shaped vertebral body at T11, and deficient posterior element of the sacrum at S4 and S5.

P5 and P6 were siblings born to consanguineous parents and belonged to the same extended family as P4 and P7. P5 had small, low set malformed ears, triangular mouth, down slanting palpebral fissures, a small nose with a depressed nasal bridge and right facial palsy. She developed recurrent respiratory infections, chronic diarrhea, severe exfoliative dermatitis and BCG-it is, and was diagnosed with Omenn syndrome. She died at eight months of age with progressive severe pneumonitis.

P6 was screened for immunodeficiency at birth because of the positive family history. She had malformed and low set small ears, small chin and protruding forehead, and generalized eczema. A skeletal survey showed central depression of the vertebral bodies in the thoracic and lumbar spine. Her immunological work up was consistent with T^- B^+ NK^+ SCID. She suffered from recurrent respiratory infections and chronic diarrhea and died at nine months of age with RSV pneumonia.

Immunological phenotype and outcome of hematopoietic stem cell transplantation (HSCT)

The main immunological findings at presentation in patients P1-P6 are shown in Table 1. In particular, P1 had significant T cell lymphopenia. His $CD4^+$ lymphocytes were largely (98%) $CD45R0^+$, no $CD4^+$ $CD45RA^+$ $CD31^+$ cells were detected, and T cell proliferation to phytohemagglutinin (PHA) was impaired (Fig. S2A). T cell receptor excision circles (TRECs) were below the limit of detection, indicating lack of thymopoiesis. TCR Vβ spectratyping revealed T cell oligoclonality (Fig. S2B). Elevated serum IgE and eosinophilia were present, consistent with an Omenn syndrome presentation.

Laboratory investigations in P2 at 2 weeks of age revealed profound T cell lymphopenia, markedly reduced proliferative response to mitogens, and increased serum IgE. An inguinal lymph node biopsy showed severe lymphoid depletion, with primary follicles without germinal centers, associated with nearly complete absence of $CD3^+$ T cells, but presence of B and NK cells and sparse plasma cells, and increased number of $CD68^+$ histiocytes and eosinophils (Fig. S3). A diagnosis of T^- B^+ NK^+ severe combined immune deficiency (SCID) was established.

Severe T cell lymphopenia was observed in P3, P4 and P6, associated with virtually absent *in vitro* T cell proliferation to PHA in P4 and P6, consistent with a diagnosis of T^- B^+ NK^+ SCID (Table 1). Finally, P5 was diagnosed as having Omenn syndrome based on generalized erythroderma, lymphocytosis, eosinophilia, hypogammaglobulinemia, increased IgE, and severely reduced *in vitro* T cell proliferation to PHA.

Because of severe immunological abnormalities, HSCT was attempted in patients P1-P4 before the gene defect was known. Details of transplant, chimerism and immune reconstitution are shown in Table 2. In all cases, a conditioning regimen was used. Two patients (P1 and P4) attained full donor chimerism. P2 failed to engraft, developed interstitial pneumonitis and died 5.5 months after HSCT. In P3, initial engraftment was followed by secondary graft failure, and a second HSCT was performed, resulting in mixed chimerism. Although three of the patients attained either full or mixed donor chimerism, none of them achieved reconstitution of the T cell compartment. In P1, who exhibits full donor chimerism, all T cells have a $CD45R0^+$ phenotype, and therefore likely represent donor-derived T cells contained in the graft that have undergone peripheral expansion. P3 attained mixed chimerism but remained with persistent severe T cell lymphopenia. She developed *Pneumocystis jiroveci* pneumonia, recurrent gastrointestinal infections, and liver failure, and died of septic shock at the age of 4 years and 7 months. P4, who attained full chimerism but failed to reconstitute T cells, developed severe autoimmune hemolytic anemia, requiring multiple courses of rituximab and immunosuppressive therapy. Altogether,

these data indicate that HSCT was unable to correct the profound T cell immunodeficiency of this disease.

Genetic studies

Prior to HSCT, karyotype analysis revealed no cytogenetic abnormalities in P1, P2, and P3. No evidence for CNV was found chromosomal microarray analysis in P1, and search for 22q11 deletion in P2 by *in situ* fluorescence hybridization was negative. No pathogenic variants in any of the known SCID-causing genes was identified in P4 by a targeted next-generation sequencing primary immunodeficiency gene panel. In an attempt to define the molecular mechanisms of the disease, whole exome sequencing (WES) was performed in P1, P2, and P4 independently (Fig. S4 and Table S1). In P1, a total of 153,376 variants were identified. Assuming autosomal recessive inheritance, and upon filtering for homozygous, rare, non-synonymous changes in coding regions and splice-sites, 38 variants were considered. Among these, functional annotation identified the *PAX1* NM_006192.3 c.463_465del variant, predicted to cause an in-frame deletion of asparagine at position 155 (p.Asn155del) of the PAX1 protein, as the most likely cause of the disease. In P2, 87,423 variants were detected. Assuming an autosomal recessive inheritance, and upon filtering for homozygous, non-synonymous, and rare (minor allele frequency <0.01) variants falling in coding regions or splice-sites, 18 such variants were considered. Functional filtering of these revealed the *PAX1* c.1104C>A variant, predicted to cause a premature termination at codon 368 (p.Cys368*), as the most likely cause of the disease. In P4, 60,772 variants were detected. Upon filtering for homozygous, non-synonymous, rare (in-house Saudi variant data base <0.005) variants, that were restricted to exonic or splice sites, and contained in an autozygome region identified on chromosome 20 by high density genotyping, and shared with P5 and P6, only 2 variants were identified, including the *PAX1* c.439G>C variant, predicted to cause a p.Val147Leu amino acid change.

Sanger sequencing confirmed homozygosity for the suspected pathogenic *PAX1* variants in P1-P6 (Fig. 1A). The Val147 and the Asn155 amino acid residues are in the DNA-binding paired-box domain, and the Cys368 residue is in the transactivation domain of the PAX1 protein (Fig. 1B). All these positions are evolutionarily conserved (Fig. S5). The scaled CADD score (CADD-Phred) for the p.Val147Leu, the p.Asn155del, and the p.Cys368* variants is 28.1, 21.2, and 38, respectively, significantly higher than the Mutation Significance Cut-off (MSC) score (9), which for the *PAX1* gene is 12.06. Altogether, these data strongly support a pathogenic role of the *PAX1* variants identified. Of note, while molecular and cellular studies to confirm the pathogenic role of the *PAX1* variants were under way, another group independently attempted WES in P3 and in other family members (but not in P2), and reported the occurrence of the p.Cys368* variant in P3 (8).

Normal subcellular localization, but reduced transactivation activity of mutant PAX1 proteins

To examine the effects of the *PAX1* variants at the protein level, we transfected 293T cells with plasmids encoding for either WT or mutant *PAX1* cDNA, and analyzed protein expression by Western blot. In this assay, we also included the PAX1 p.Gly166Val variant which had been previously reported in a patient with OTFCS2 (6). As shown in Fig. 2A, all

mutant proteins were expressed at similar levels as WT PAX1, with the p.Cys368* mutant migrating as a lower molecular weight (MW) product, as predicted. To check whether the identified variants altered the subcellular localization of the PAX1 protein, 293T cells were transfected with PAX1 constructs with an N-terminus HA tag, and immunofluorescence was performed with TRITC-conjugated anti-HA antibody. As shown in Fig. 2B, both wild-type (WT) and mutant PAX proteins were detected in the nucleus, indicating that these variants do not affect subcellular localization.

Next, we tested the transcriptional activity of the PAX1 mutant proteins. Little is known on transcriptional targets of human PAX1, however the *Nkx3–2* promoter has been identified as a PAX1 target in mice (10). Therefore, we generated a reporter system in which luciferase expression is driven by the mouse *Nkx3*-2 promoter. In parallel, we generated either WT (Pax1^{WT}) or mutant (*Pax1*^{Val138Leu}, *Pax1*^{Asn146del}, *Pax1*^{Cys359*}, *Pax1*^{Gly157Val}) N-terminus HA-tagged mouse *Pax1* constructs, which encode for mouse mutant PAX1 proteins corresponding to the human p.Val147Leu, p.Asn155del, p.Cys368*, and p.Gly166Val variants, respectively. Western blot analysis confirmed that the mutant mouse PAX1 proteins were expressed at similar levels as WT PAX1 (Fig. S6). Upon co-transfection of the *Nkx3.2*-luciferase reporter plasmid and of either WT or mutant PAX1 expression plasmids into 293T cells, analysis of luciferase activity showed that the p.Val138Leu, the p.Asn146del, and the p.Cys359* PAX1 mutant proteins had significantly reduced reporter expression, when compared to WT PAX1 (Fig. 2C and raw data file S1). A similar defect was also observed for the p.Gly157Val mutant, confirming previous findings (6). These data suggest that the human p.Val147Leu, p.Asn155del and p.Cys368* variants do not affect protein stability or subcellular localization but alter PAX1 transcriptional activity.

Molecular modeling

The structure of the human PAX1 protein has not been solved experimentally. However, a crystal structure is available for the paired-box domain of the highly homologous PAX6 protein (11). Sequence alignment between the paired-box domain of PAX6 and PAX1 proteins reveals a high level of conservation with a similarity of 71% with a 100% coverage of the region to be modelled as calculated with the BLOSUM80 matrix from PSI-BLAST (E value= 1.3691e-20). As reported by Kelm et al (12), this degree of homology often yields a model for the target (PAX1) with an accuracy of less than 1 Å root mean square deviation (RMSD) of atomic mobility to the experimentally solved structure of the template (PAX6). Because the p.Val147Leu and p.Asn155del mutants fall within the paired-box domain of the protein, we assessed whether the reduced functional activity of the mouse p.Val138Leu and p.Asn146del (and by inference, the human p.Val147Leu and p.Asn155del) variants results from an altered structure and/or abnormal DNA binding. To do this, we first developed a structural model of the paired-box domain of WT and mutant PAX1 bound to DNA, based on its homology to the published crystal structure of PAX6 (PDB: 6PAX) (11) by the satisfaction of spatial restraints method using Modeler (13). Structural alignment revealed that the paired-box domains of the PAX1 and PAX6 proteins are almost identical with a template modeling (TM) score of 0.99963 and RMSD of 0.08 Å as measured by the TM align algorithm (14). In addition, the high quality of the model is reflected by the fact that 99% of the residues are in the allowed regions of the φ (phi) *vs.* ψ (psi) angles of the

Ramachandran Plot as shown in Fig. S7 (15). Therefore, we used this model to derive a corresponding model for the p.Val147Leu, p.Asn155del and for the previously described p.Gly166Val PAX1 variants (6), using *in silico* site-directed mutagenesis and energy minimization refinement as previously described (16). As shown in Fig. 3A, the paired-box domain of all three mutant PAX1 proteins retains a structure composed of two globular domains separated by a linker. These structural models were then used in MD simulations for both their free and DNA-bound forms to define how they differ in both structure and time-dependent dynamic behavior from the canonical WT PAX1 protein.

MD Simulation of the Unbound PAX1 Variants

Since the p.Val147Leu variant is located in the first globular domain, the p.Asn155del is also located in this domain and adjacent to the highly flexible linker, while the p.Gly166Val variant is within the linker, we initially performed 200 picoseconds (ps) MD simulations of PAX1 in the absence of DNA to capture potential alterations of the rapid movement of this region of the protein in relationship to the N- and C-terminal helix-loop-helix domains. To gain additional insights into the behavior of the protein, we extended these simulations to 10 nanoseconds (ns), both in the absence or presence of DNA. When a harmonic restraint is applied to reduce the conformational changes in both globular domains during the 200 ps simulation, the linker is observed to move freely. In this situation, the molecular movement of WT PAX1 paired-box domain resembles a barbell-shaped harmonic oscillator where the globular domains move relative to each other without forming bonds that lock them together in space.

At the end of the 200 ps, in the absence of DNA, the linker of PAX1 shortens and the protein populates a conformational landscape where the globular domains come in close proximity of each other with the linker located between the N-terminal helix 3 (H3) and the C-terminal helix 1 (H1), respectively (Fig. S8). In fact, in the most extended conformation of the linker, the inter-globular domain distance measured from the Gly158 alpha-C to the Pro175 alpha-C shortens from an original 38.946 Å to 21.414 Å (SD= 2.421, p= 0.0001). This shortening contributes to the differences in the RMSD curve, where in the first part of the simulation we observed significant changes due to this shortening, whereas the difference in conformational sampling decreases toward the end of the run. Identical results were obtained in 10 ns simulations. Thus, this H3-Linker-H1 state is likely the one that the PAX1 binding domain adopts when in conformational equilibrium before binding to DNA. In this manner, the linker would be free to contact the minor groove of the DNA and extend in a manner that allows the positioning of both globular domains for full binding. These results led us to set up simulations that would enable gathering information on potential differences in DNA binding among the WT and mutant PAX1 variants.

Molecular Modeling and Dynamic Simulation of the PAX1 Variants Bound to DNA

To investigate whether alterations in the structure or the dynamics of the PAX1 variants have the potential to impact the protein function as a transcription factors, we modeled these proteins in complex with DNA. For this purpose, we again used the bound form of PAX6 as a template. Fig. S9 shows the energy minimized structure of these models before MD simulations. Since the variants identified in the patients either change the sequence of the

linker (p.Gly166Val) or the N-terminal globular domain (p.Val147Leu, p.Asn155del), we compared the structures of these variants with WT PAX1 after MD simulation. As the structure of the DNA interacting with wild-type or mutant PAX1 proteins was the same in all models shown in Fig. S9, we removed it to facilitate the observation of changes that occur in the PAX1 polypeptide chain. When compared to WT PAX1, the p.Val147Leu and the p.Asn155del variants associated with OTFCS2+SCID differ in particular at the C-terminal second globular domain, as shown by molecular superimposition (Fig. 3B). This result is consistent with the measured root mean square fluctuation (RMSF) values, which shows that the second globular domain is highly flexible in the p.Val147Leu and p.Asn155del mutant proteins (Fig. 3C). By contrast, RMSF values in the first globular domain were lower in all mutant proteins (and especially so in the p.Asn155del and p.Gly166Val mutants) as compared to WT PAX1. Considering these changes, we evaluated potential alterations in the ability of these proteins to recognize and bind to DNA *in silico*. For this purpose, we analyzed the PAX1-DNA interface. As shown in Fig. 4, as compared to WT PAX1, a lower number of amino acid residues contacting DNA were present within the paired-box domain of the p.Val147Leu and p.Asn155del PAX1 mutants. These alterations are more pronounced for the C-terminal region of the domain, which contacts the 3' half of the oligonucleotide, and is necessary to maintain appropriate binding to DNA. This altered pattern of interaction with DNA observed *in silico* may contribute to the altered transcriptional activity of the PAX1 mutant proteins.

Differential gene expression profile upon in vitro differentiation of control- and patient-derived iPSCs to TEP cells

To gain insights into how pathogenic *PAX1* variants may perturb the developmental program of TECs, we reprogrammed fibroblasts from a healthy control, patient P1 and patient P4 to iPSCs, and subsequently differentiated these to TEP cells using a previously published protocol (17) with some modifications (see: Materials and Methods). Quantitative real-time PCR (qRT-PCR) showed a comparable stemness profile in both control and patient iPSCs (Fig. S10), and cytogenetic analysis confirmed their karyotypic integrity. iPSCs were then exposed *in vitro* to a cocktail of growth factors and molecules that provide essential cues to allow differentiation into definitive endoderm (DE) and eventually into TEP cells (Fig. S11A).

To assess changes in the gene expression profile of cells during differentiation, we performed RNA sequencing (RNA-seq) in control cells collected in triplicate at iPS (day 0), DE (day 5), and TEP (day 14) stages of cell differentiation. For each condition, between 15 and 20 million reads were obtained per well. As shown in Fig. S11B, during differentiation of control iPS cells to DE and TEPs, we observed progressive changes of gene expression profile, with increased expression of stemness (*OCT4, MYC, SOX2, TERT, DNMT3B, NANOG*), endoderm (*EOMES*, *CXCR4*, *SOX17*) and epithelial (*KRT8, CLDN1, EPCAM*, *LAMA1*, and *KRT19*) genes at iPS, DE, and TEP stages, respectively. In addition, expression of *ASXL1, HES1, SHH, GATA3, HOXA3*, *PSEN1*, *ZBTB1*, *HAND2* and *MAFB* genes, which are all part of the gene set "Thymus development", was upregulated at TEP stage (Fig. S11B). Gene set enrichment analysis (GSEA) confirmed differential expression of genes involved in somatic cell maintenance, endoderm development, as well as in other

pathways related to differentiation of tissues derived from the third and fourth pharyngeal pouches (Fig. S11C).

To assess the reproducibility of the differentiation protocol, the same control iPS line was differentiated twice to TEP cells (named C1 and C2, respectively) in parallel to differentiation of P1 and P4 iPS cells to TEP cells in two distinct differentiation experiments. As shown in Fig. 5A, a similar pattern of changes in the gene expression profile was observed when differentiating control (C1) and P1 iPS cells, or control (C2) and P4 iPS cells to TEP cells. In both experiments, control and patient cells showed increased expression of stemness genes at the iPS stage, whereas enhanced expression of epithelial marker genes and of other genes included in the “Thymus development” gene set was detected at TEP stage. Furthermore, immunohistochemistry analysis confirmed that both control and P1 TEP cells expressed cytokeratin 8 (KRT8), a marker of thymic epithelial cells (Fig. S12) (18).

GSEA confirmed that upon differentiation of control iPS cells to TEP cells, genes involved in thymus development were more abundantly expressed at the TEP stage both in control and in PAX1 mutant cells (Fig. 5B). Despite similar changes in gene expression profile during differentiation of control- and patient-derived iPS cells to TEP cells, GSEA demonstrated that genes involved in thymus development were more abundantly expressed in control than in patient TEP cells (Fig. 5C). To gain additional mechanistic insights into the severe T-cell immunodeficiency of P1 and P4, we performed multiple rounds of differentiation of control and patient iPS cells to TEP cells (5 times for control and P1, and four times for control and P4 cells, respectively), and utilized qRT-PCR to analyze the expression of *FOXN1,* a master regulator of TEC development (19, 20), and to its target DLL4, a Notch ligand that plays a critical role in T-cell commitment (21). *FOXN1* expression was significantly reduced in P1 and P4 TEPs as compared to control cells, and a similar trend was observed for *DLL4*, although for the latter significance was reached only when comparing P1 to control TEPs (Fig. 5D and raw data file S1). Analysis of RNA-seq data revealed several other genes that showed concordantly reduced expression in P1 and P4 TEPs versus control TEPs, reaching statistical significance in at least one of the patients’ TEP lines (Fig. 5E and Table S2). These included *STC2, CD83, ZAR1* and *ANKMY1*, which are known FOXN1 target genes (19); *TP63*, a regulator of TEC proliferation and ageing (22, 23); *BMP4*, which has been implied in thymus development (24, 25) and in maintenance of TEPs (26, 27); and *EYA1* and *PAX9*, which are involved in patterning of pharyngeal endoderm (28, 29). Altogether, these data indicate that multiple mechanisms contribute to the thymic defects associated with PAX1 deficiency. Consistent with this, and with the syndromic features manifested by the patients, we observed that several genes included in the “Neural crest cell differentiation”, ”Ear development”, “Cartilage development”, “Pharyngeal system development” and “Skeletal system development” gene sets, also manifested differential expression in P1 and P4 versus control TEPs (Fig. S13).

Discussion

We have studied six patients from three unrelated families in whom biallelic, loss-of-function *PAX1* variants underlie a clinical phenotype characterized by OTFCS2 and severe T

cell immunodeficiency. The first example of a biallelic, rare *PAX1* variant (p.Gly166Val) in a patient with autosomal recessive OTFCS2 was provided by Pohl et al. (6), who also showed reduced transcriptional activity of the mutant PAX1 protein. However, no data on the patient's immunological phenotype were provided. More recently, Patil et al. have described two siblings with a homozygous frameshift *PAX1* variant causing OTFCS2; one of them lacked a thymic shadow on chest X-ray (7). Finally, the clinical features of OTFCS2 and SCID has been recently reported by Paganini et al. in two of the patients studied herein (P2 and P3), but no immunological or mechanistic characterization was provided (8).

Several mouse models of PAX1 deficiency, due to distinct variants in the *Pax1* gene, have been described, including the *undulated* (*un*), *undulated extensive* (un^{ex}), *undulated short-tail* (un^{S}), and *undulated intermediate* (*un-i*) models (30). All of these mutant strains display thymic abnormalities, which are more severe in the un^{S} model (30); however, none of them results in complete athymia. A more profound phenotype, with lack of thymus and parathyroids, associated with craniofacial and skeletal abnormalities, has been observed in $Pax9^{-/-}$ mice (31). No cases have been reported of humans with biallelic *PAX9* pathogenic variants, and heterozygous *PAX9* variants in humans are associated with hypodontia, but not with thymic defects (32). Together, these data suggest that the impact of PAX1 and PAX9 on thymus development may be different in humans and mice.

To gain insights into the molecular mechanisms by which PAX1 deficiency may cause syndromic SCID in humans, we have first investigated the expression, subcellular localization and transactivation activity of PAX1 mutant proteins using transient transfection and luciferase reporter studies. Although transient transfection may result in protein overexpression and therefore cannot be directly compared to protein expression *in vivo*, the PAX1 p.Val147Leu, p.Asn155del, and p.Cys368* mutant proteins retained the capacity to translocate to the nucleus, and the equivalent murine mutant proteins showed decreased transcription factor activity *in vitro*. Similar results were obtained for the PAX1 p.Gly166Val (and the mouse equivalent p.Gly157Val) variants, confirming previous observations (6). To further investigate the mechanisms underlying the impaired transcriptional activity of the mutant PAX1 proteins, we have performed structural modeling, using the crystal structure of the PAX6 paired-box domain as a template. The results suggest that the structural behavior of the paired-box domain (consisting of two globular domains interconnected by a linker) was retained in the p.Val147Leu, p.Asn155del, and p.Gly166Val mutants. MD simulation studies have demonstrated that these variants alter the flexibility of the paired-box domain and are predicted to alter binding of PAX1 to its target DNA. Interestingly, our *in silico* studies suggest that the mutants differ in their ability to gain or lose binding to distinct nucleotides, with possible impact on the severity of clinical and immunological phenotype. Fine characterization of the molecular mechanisms underlying such heterogeneity will require resolution of the crystal structure of the PAX1 paired-box domain and precise identification of its human DNA target sequence(s).

By exposing control- and patient-derived iPSCs to defined differentiation cues, we have successfully differentiated iPSCs to TEPs. Comparison of gene expression profile in control- and patient-derived cells at the TEP stage of *in vitro* differentiation, demonstrated altered expression of genes involved in thymus development in patient cells. In particular, qRT-PCR

analysis revealed reduced expression of *FOXN1*, a master gene of thymus development, and of several FOXN1-target genes, including *DLL4*. Bi-allelic *FOXN1* pathogenic variants in humans are responsible for a syndromic form of SCID that is the equivalent to what observed in the “nude” mouse (33, 34). We have recently reported that *FOXN1* haploinsufficiency in humans causes severe T-cell lymphopenia at birth (35). The reduced levels of *FOXN1* expression observed in patient TEPs (and by inference, in the patients’ thymus) may therefore play a direct role in the severe T-cell lymphopenia observed in these patients. However, analysis of gene expression profile in patient and control TEPs suggest that other mechanisms, besides reduced *FOXN1* expression, may also contribute to impaired thymic development associated with PAX1 deficiency. In particular, reduced *TP63* expression may cause impaired TEC proliferation and hence thymic hypoplasia. Moreover, we observed that both P1 and P4 TEPs displayed significantly reduced expression of *BMP4* as compared to control TEPs. Conditional deletion of *Bmp4* from the pharyngeal endoderm prior to *Foxn1* expression disrupts thymus morphogenesis in mice (24). Furthermore, recent studies have indicated that BMP4 plays a critical role in maintenance of TEC progenitors (27), and reduced BMP4 expression might alter replenishment of the TEC compartment. Future studies based on precise enumeration of TEPs generated in vitro from patient and control-derived iPSCs may help test this hypothesis. In any case, these data suggest that PAX1 deficiency causes early and more global effects on the development of tissues derived from the third and fourth pharyngeal pouches, including the thymus. Consistent with this hypothesis, patient TEPs were concordant in the abnormal expression of a number of genes involved in skeletal, cartilage, pharyngeal, neural crest and ear development. Abnormalities in these pathways during differentiation of tissues derived from the third and fourth pharyngeal pouches are likely to contribute to the broad range of malformations observed in the patients reported here.

Finally, we have reported that HSCT, which was attempted in four of the six patients, failed to correct the T cell immunodeficiency, despite engraftment in three of them. PAX1 deficiency should be added to the list of severe T cell immunodeficiencies characterized by a primary thymic defect, which also includes complete DiGeorge syndrome, CHARGE syndrome, and *FOXN1* deficiency (1). Thymus transplantation represents the treatment of choice to correct the immunodeficiency in these disorders (36–38). By contrast, use of unmanipulated HSCT may allow engraftment of donor-derived post-thymic T cells that may expand in the recipient, as also observed in P1 in this study, but does not permit *de novo* generation of a polyclonal repertoire of naïve T cells (39).

In summary, we have provided mechanistic insights into the pathophysiology of OTFCS2 associated with severe T cell immunodeficiency, an autosomal recessive condition caused by *PAX1* variants, and have demonstrated the thymic-intrinsic nature of the immunodeficiency of this condition.

Study Design

The scope of the study was to identify the molecular basis of a syndromic form of SCID, and to perform genomic, molecular, biochemical, structural modeling and in vitro disease modeling studies to analyze deleterious effects of the *PAX1* variants identified. All patients

provided written informed consent, according to protocols approved by the local Institutional Review Boards (IRBs). Research studies were performed under NIH IRB-approved protocol 16-I-N139. For patient P4, public disclosure of secondary genomic findings was not permitted by the protocol and consent form approved by the local IRB.

Materials and Methods

Genetic Studies

WES was performed on P1 and his healthy parents, and on P2 and P4 without parental samples. Detailed methods for capture, library preparation, and bioinformatic analysis are described in the Supplementary Material. Candidate variants were confirmed by Sanger sequencing, and described according to Human Genome Variation Society (HGVS) guidelines. For patients P1 and P2, WES data have been deposited to the NCBI SRA Submission Portal, with the following ID: PRJNA601119.

Immunological studies

Flow cytometry studies were performed on either a 10-color Gallios® (Beckman Coulter, Brea, CA) or an eight-color Canto II (BD BioSciences, San Jose, CA) cytometer, and results were analyzed using Kaluza software v1.5 (Beckman Coulter, Brea, CA). T cell proliferation studies were performed using Edu®-based (Thermo Fisher Scientific, Waltham, MA) flow cytometry method in P1, and tritiated thymidine (^{3}HTdR) incorporation in P2, P4, P5 and P6. TCR Vβ repertoire spectratyping was carried out using a fragment-length method on a capillary electrophoresis system (ABI 3730xl DNA Sequencer, Applied Biosystems Inc., Thermo Fisher, Waltham, MA), and data were analyzed using the Gene Marker® (v.2.4.0) software (SoftGenetics, State College, PA). All reference values for interpretation were established in the laboratory using healthy pediatric donors recruited via an IRB-approved protocol.

Western blot analysis and confocal immunofluorescence

293T cells were plated as 4×10^{5} cells per well in a 12-well-plate. After 24 h, cells were transfected with 1.2 μg of pCMV-HA-N vector containing either wild-type (WT) or mutant *PAX1* cDNAs, with the Lipofectamine 3000 transfection kit (Thermo Fisher Scientific) following manufacturer's instructions. After 24 h, cells were collected, lysed, and transferred onto a nitrocellulose membrane. Immunoblotting was performed with rat anti-PAX1/Pax1 monoclonal antibody (mAb) (clone 5A2) (40), followed by staining with HRP-conjugated goat anti-rat IgG (ab97057, Abcam, Cambridge, MA). After stripping, the membrane was re-blotted with rabbit anti-β-actin mAb (clone 13E5, Cell Signaling Technology, Danvers, MA) followed by Amersham ECL anti-rabbit IgG, HRP linked whole antibody (NA934, GE Heath care, Helsinki, Finland).

To analyze PAX1 subcellular localization, 293T cells were cultured in polylysine-coated μ−Slide 8 well (ibidi, Fitchburg, WI) and transfected with 100 ng of pCMV-HA-N vector containing either wild-type or mutant PAX1 cDNA, with the Lipofectamine 3000 transfection kit (Thermo Fisher Scientific) following manufacturer's instructions. After 24 h, cells were fixed in 4% paraformaldehyde with PBS for 30 min at room temperature, washed

twice in PBS, and then blocked for 1 hour with 10% donkey serum and 0.1% Triton X with PBS at room temperature. Cells were incubated with mouse anti-HA-TRITC monoclonal antibody (clone H9037; Millipore-Sigma, St. Louis) diluted 1:200 in PBS, and with DAPI at room temperature for 1 h in the dark. Images were obtained with a Leica SP8 (690/730) confocal microscope.

For immunofluorescence analysis of KRT8 expression by TEPs, cells were fixed in 4% paraformaldehyde with PBS for 30 min at room temperature, washed twice in PBS, blocked for 1 hour in 10% Donkey serum and 0.1% TritonX with PBS at room temperature, and incubated overnight at 4°C with mouse anti-Cytokeratin 8 antibody (ab2530, C-43) (Abcam, Cambridge, MA) diluted 1:200 in PBS, then for 1 h at room temperature in the dark with donkey-anti-mouse IgG H and L Alexa Fluor 488 (ab150105, Abcam) at 1:500 dilution in PBS, and with DAPI (Thermo Fisher Scientific) at 1:1000 dilution in PBS. Images were taken with Leica SP8 (690/730) confocal microscope.

Generation of Nkx3–2 and Pax1 constructs and analysis of Pax1 transcriptional activity

The promoter region of the mouse *Nkx3–2* gene was amplified and cloned into the firefly reporter plasmid pGL4.10 luc2 vector (Promega, Madison, WI), as described (6, 10). To generate expression plasmids containing the mouse *Pax1*^{WT}, *Pax1*^{V138L,} *Pax1*^{N146del}, *Pax1*^{G157V}, and *Pax1*^{C359*} coding sequences, the coding sequence of mouse *Pax1* (NM_008780.2), was amplified by RT-PCR from isolated adult mouse thymus RNA, and cloned into a pCMV-HA-N vector (Addgene, Cambridge, MA) with the In-Fusion HD EcoDry Cloning Kit (Clontech, Mountain View, CA). *Pax1* mutant variants were generated by site-directed mutagenesis, and the PCR products were ligated with the Quick ligation kit (NEB, Ipswich, MA) and cloned by Turbo competent cells (NEB, Ipswich, MA). The correct sequence of the constructs was confirmed by Sanger sequencing.

The transcriptional activity of WT and mutant PAX1 mouse proteins was assessed in a luciferase reporter assay. 293T cells were cultured in Dulbecco's modified Eagle media (DMEM) containing 10 % fetal bovine serum (FBS) with antibiotics and plated in 24-well plates 24 h prior to transfection. Transient transfections were performed in triplicate with TransIT-293 Reagent (Mirus, Madison, WI) according to manufacturer's instructions. Cells were co-transfected with 30 ng of either WT or mutant *Pax1* expression plasmids, 15 ng of firefly reporter plasmid *Nkx3–2*-pGL4.10 luc2, and 3 ng of pRL-TK vector (Promega, Madison, WI) for normalization. After 48 h, cell extracts were collected and frozen in lysis buffer overnight at - 20°. After thawing, firefly and renilla luciferase activities were measured using a Dual Luciferase Reporter Assay Kit (Promega, Madison, WI) and PARADIGM Detection platform (Beckman Coulter, Indianapolis, IN). To correct for variations in transfection efficiency, firefly luciferase activity was normalized to renilla luciferase activity. The luciferase activity of pCMV-HA-N vector which had no *Pax1* cDNA was assumed to have 0% activity, whereas the Pax1^{WT} vector was assumed to have 100% activity.

Molecular Modeling and MD Simulation

The three-dimensional complex structures of WT and mutant PAX1 models bound to DNA were generated by homology-based methods (16) using the previously solved structure of the highly homologous protein, PAX6 (PDB: 6PAX) (11). Intermolecular interactions of the PAX1 paired-box domain of WT/mutant PAX1 to DNA complex were calculated in the Receptor-Ligand function of Discovery Studio Client 4.0 using the default parameters (BIOVIA, San Diego, CA). The MD simulations were performed as described (16).

Generation and targeted differentiation of induced pluripotent stem cells (iPSCs)

Primary skin fibroblasts from P1, P4, and a healthy control (BJ fibroblast line, ATCC) were reprogrammed to iPSCs by infection with the non-integrating CytoTune Sendai viral vector kit (Thermo Fisher Scientific) as described (41).

For differentiation, iPSCs were transferred to plates coated with Corning Matrigel hESC-qualified Matrix. After 4–5 passages, the cells were plated on Matrigel-coated 24-well plates at a density of 2.5×10^5 cells/cm^2. For differentiation to definitive endoderm (DE) and TEPs, iPSCs were exposed to various factors and differentiation cues, according to the protocol by Parent et al (17), with some modifications. In particular, between day 1 to day 5 (d1-d5), iPSC differentiation was carried out in RPMI 1640 medium (Thermo Fisher Scientific, Waltham, MA) supplemented with 1% penicillin/streptomycin, 1% L-glutamine, and increasing concentrations of KSR (0% on d1, 0.2% on d2–d3, and 2% on d4-d5). In the period d6-d14, cells were differentiated in DMEM/F12 with 1% penicillin/streptomycin, 1% L-glutamine, 0.5% v/v B-27 supplement (Thermo Fisher Scientific, Waltham, MA). During this period of time, the following factors were added to the culture: activin A, 100 ng/ml (d1–d5); Wnt3a, 25 ng/ml (d1) or 50 ng/ml (d8–d14); all-trans retinoic acid (RA), 0.25 μM (d6–d8) or 0.1 μM (d9–d14); BMP4, 50 ng/ml (d6–d14); LY364947, 5 mM (d6–d9); FGF8b, 50 ng/ml (d8–d14); and KAAD-cyclopamine, 0.5 mM (d8–d14). Supplements and factors were from Thermo Fisher Scientific, Waltham, MA (B27, KSR); R&D Systems, Minneapolis, MN (activin A, Wnt3a, BMP4, and FGF8b); and, Millipore-Sigma, St. Louis, MO (RA, KAAD-cyclopamine, LY364947).

Transcriptome profiling by RNA-sequencing, data processing, and differential expression analysis

Microgram quantities of total RNA were isolated using the RNeasy kit (QIAGEN, Hilden, Germany) from triplicate samples of control-, P1- and P4-derived iPSCs, as well as from the corresponding iPSC-derived cells at DE, and TEP stages. RNA integrity was tested by microfluidic electrophoresis on a TapeStation system (Agilent, Santa Clara, CA). RNA purity and concentration were assessed using the Nanodrop One UV-Vis Spectrophotometer (Thermo Fischer Scientific, Waltham, MA). Directional, mRNA-seq libraries for Experiment 1 were produced using TruSeq Stranded mRNA Library Prep Kit for NeoPrep (Catalog # NP-202–1001) from Illumina (San Diego, CA). Directional, mRNA-seq libriaries for Experiment 2 were produced using NewEngland Biolabs product NEBNext Poly(A) mRNA Magnetic Isolation Module (catalog #E7490L), New England Biolabs product NEBNext® Ultra™ II Directional RNA Library Prep Kit for Illumina (catalog #E7760L), and NEBNext

Multiplex Oligos for Illumina® (Dual Index Primers Set 1) (catalog #E7600S) (New England Biolabs, Ipswich MA), with an input of 100 ng total RNA per sample.

Sequencing was performed on an Illumina NextSeq 500 system, running Illumina NextSeq Control Software System Suite version 2.1.2 and RTA version 2.4.11. The final library pool was sequenced via 1 × 75 bp run configuration using the product NextSeq 500/550 High Output v2 sequencing kit, 75 cycles (Catalog # FC-404–2005). Between 15 and 20×10^6 reads were obtained from each sample. RNA-seq FASTQ files were aligned to the reference human genome assembly (GRCh38) with STAR v2.6.0 (42). The transcript annotation (GTF) file was obtained from GENCODE (release 28) (43). The binary alignment files (.bam) were then used to generate a matrix of read counts with the featureCounts program of the package Subread v.1.6.2 (44). Exonic fragments were grouped at the level of genes, based on the GENCODE 28 annotation file. Normalization and differential expression analysis for RNA-seq data were performed with the DESeq2 (45) package in R (46).

Independent pairwise analyses were performed on triplicate samples of cells at each stage of differentiation (iPSC, DE, and TEP). To handle the lower power associated with small numbers of samples, DESeq2 employs an empirical Bayesian procedure to stabilize the log-fold change estimates. The Wald test was then applied to the log-fold change in each gene, followed by multiple-testing adjustment with the method of Benjamini and Hochberg (47).

For the heatmap of gene expression, t-test and hierarchical clustering were computed by Qlucore Omics Explorer 3.3 (Qlucore, Lund, Sweden) for iPSC and TEP stage comparison (Figure 5A), with cut-off q values less than 0.01. ANOVA and hierarchical clustering were used for the three-stage (iPSC, DE, TEP) comparison (Supplementary Figure 11B). Normalization and differential expression analysis of the RNA-seq data used for Gene Set Enrichment Analysis (GSEA) were performed with DESeq2 package in R v.3.5.1. RNA-sequencing data have been uploaded to the National Center for Biotechnology Information (NCBI) Gene Expression Omnibus (GEO), under accession no. GSE138784.

Gene Set Enrichment Analysis

GSEA was performed with the GSEA software (48) (http://www.broadinstitute.org/gsea) using a pre-ranked dataset of gene expression differences, 1000 permutations, and the software's classic enrichment statistic option. Genes were ranked based on the DESeq2 output, by taking the signed -log10 adjusted p value for differential expression. Gene sets for enrichment analysis correspond to Gene Ontology (GO) Biological Processes and were obtained from the Molecular Signatures Database, version 7.0 (GMT file: c5.bp.v7.0.symbols.gmt).

qRT-PCR

RNA was isolated from control, P1, and P4 cells at iPSC and TEP stages of differentiation, using RNeasy kit (QIAGEN, Hilden, Germany). cDNA was synthesized by a qScript cDNA Synthesis kit (Quantabio, Beverly, MA) according to the manufacturer's protocol. Quantitative real-time PCR was performed on a 7500 Real Time PCR System (Applied Biosystems, Waltham, MA) using PerfeCTa SYBR Green Fast-Mix, Low ROX (Quantabio,

Beverly, MA). Gene expression was quantified by normalization to the housekeeping gene TBP for each sample.

Primers used for individual genes are reported in the Supplementary Material.

Statistical analysis

Statistical analysis was undertaken in GraphPad Prism (v8.0). For luciferase reporter assay, P values were calculated with one-way ANOVA, and adjusted by Dunnett's multiple comparisons test. The data are means ± SEM of 6 independent experiments (WT, n=6; Val138Leu, n=3; Asn146del, n=5; Cys359*, n=5; Gly157Val, n=5; empty, n=6). For qRT-PCR data, Student's *t* test (paired, two-tailed) was performed. The data are means ± SEM in Fig 5D, and means ± SD in Fig S10. $P<0.05$ was considered to be significant. Statistical analysis of RNA-seq data is described above.

Supplementary Material

Refer to Web version on PubMed Central for supplementary material.

Acknowledgments

We thank Dr. Erik Thorland for interpretive assistance with the CNV analysis and Benedetta Bigio, M.S. for uploading WES data. WES data have been deposited to the NCBI SRA Submission Portal, with the following ID: PRJNA601119. RNA-sequencing data have been uploaded to the National Center for Biotechnology Information (NCBI) Gene Expression Omnibus (GEO), under accession no. GSE138784.

Funding: This work was supported by the Division of Intramural Research, National Institute of Allergy and Infectious Diseases, National Institutes of Health, and by the "Angelo Nocivelli" Foundation. Yasuhiro Yamazaki was supported by JSPS Research Fellowship for Japanese Biomedical and Behavioral Research at NIH, and had travel support from The ITO Foundation for the Promotion of Medical Science.

References

1. Picard C, Bobby Gaspar H, Al-Herz W, Bousfiha A, Casanova JL, Chatila T, Crow YJ, Cunningham-Rundles C, Etzioni A, Franco JL, Holland SM, Klein C, Morio T, Ochs HD, Oksenhendler E, Puck J, Tang MLK, Tangye SG, Torgerson TR, Sullivan KE, International Union of Immunological Societies: 2017 Primary Immunodeficiency Diseases Committee Report on Inborn Errors of Immunity. J Clin Immunol 38, 96–128 (2018). [PubMed: 29226302]
2. Farley AM, Morris LX, Vroegindeweij E, Depreter ML, Vaidya H, Stenhouse FH, Tomlinson SR, Anderson RA, Cupedo T, Cornelissen JJ, Blackburn CC, Dynamics of thymus organogenesis and colonization in early human development. Development 140, 2015–2026 (2013). [PubMed: 23571219]
3. Balling R, Deutsch U, Gruss P, *undulated*, a mutation affecting the development of the mouse skeleton, has a point mutation in the paired box of *Pax 1*. Cell 55, 531–535 (1988). [PubMed: 3180219]
4. Dietrich S, Gruss P, *undulated* phenotypes suggest a role of *Pax-1* for the development of vertebral and extravertebral structures. Dev Biol 167, 529–548 (1995). [PubMed: 7875377]
5. Adham IM, Gille M, Gamel AJ, Reis A, Dressel R, Steding G, Brand-Saberi B, Engel W, The scoliosis (sco) mouse: a new allele of *Pax1*. Cytogenet Genome Res 111, 16–26 (2005). [PubMed: 16093716]
6. Pohl E, Aykut A, Beleggia F, Karaca E, Durmaz B, Keupp K, Arslan E, Palamar M, Yigit G, Ozkinay F, Wollnik B, A hypofunctional PAX1 mutation causes autosomal recessively inherited otofaciocervical syndrome. Hum Genet 132, 1311–1320 (2013). [PubMed: 23851939]

7. Patil SJ, Das Bhowmik A, Bhat V, Satidevi Vineeth V, Vasudevamurthy R, Dalal A, Autosomal recessive otofaciocervical syndrome type 2 with novel homozygous small insertion in *PAX1* gene. Am J Med Genet A 176, 1200–1206 (2018). [PubMed: 29681087]
8. Paganini I, Sestini R, Capone GL, Putignano AL, Contini E, Giotti I, Gensini F, Marozza A, Barilaro A, Porfirio B, Papi L, A novel *PAX1* null homozygous mutation in autosomal recessive otofaciocervical syndrome associated with severe combined immunodeficiency. Clin Genet 92, 664–668 (2017). [PubMed: 28657137]
9. Itan Y, Shang L, Boisson B, Ciancanelli MJ, Markle JG, Martinez-Barricarte R, Scott E, Shah I, Stenson PD, Gleeson J, Cooper DN, Quintana-Murci L, Zhang SY, Abel L, Casanova JL, The mutation significance cutoff: gene-level thresholds for variant predictions. Nat Methods 13, 109–110 (2016). [PubMed: 26820543]
10. Rodrigo I, Hill RE, Balling R, Munsterberg A, Imai K, Pax1 and Pax9 activate Bapx1 to induce chondrogenic differentiation in the sclerotome. Development 130, 473–482 (2003). [PubMed: 12490554]
11. Xu HE, Rould MA, Xu W, Epstein JA, Maas RL, Pabo CO, Crystal structure of the human Pax6 paired domain-DNA complex reveals specific roles for the linker region and carboxy-terminal subdomain in DNA binding. Genes Dev 13, 1263–1275 (1999). [PubMed: 10346815]
12. Kelm S, Shi J, Deane CM, MEDELLER: homology-based coordinate generation for membrane proteins. Bioinformatics 26, 2833–2840 (2010). [PubMed: 20926421]
13. Sali A, Blundell TL, Comparative protein modelling by satisfaction of spatial restraints. J Mol Biol 234, 779–815 (1993). [PubMed: 8254673]
14. Zhang Y, Skolnick J, TM-align: a protein structure alignment algorithm based on the TM-score. Nucleic Acids Res 33, 2302–2309 (2005). [PubMed: 15849316]
15. Ramachandran GN, Ramakrishnan C, Sasisekharan V, Stereochemistry of polypeptide chain configurations. J Mol Biol 7, 95–99 (1963). [PubMed: 13990617]
16. Velez G, Lin M, Christensen T, Faubion WA, Lomberk G, Urrutia R, Evidence supporting a critical contribution of intrinsically disordered regions to the biochemical behavior of full-length human HP1gamma. J Mol Model 22, 12 (2016). [PubMed: 26680990]
17. Parent AV, Russ HA, Khan IS, LaFlam TN, Metzger TC, Anderson MS, Hebrok M, Generation of functional thymic epithelium from human embryonic stem cells that supports host T cell development. Cell Stem Cell 13, 219–229 (2013). [PubMed: 23684540]
18. Klug DB, Carter C, Crouch E, Roop D, Conti CJ, Richie ER, Interdependence of cortical thymic epithelial cell differentiation and T-lineage commitment. Proc Natl Acad Sci U S A 95, 11822–11827 (1998). [PubMed: 9751749]
19. Zuklys S, Handel A, Zhanybekova S, Govani F, Keller M, Maio S, Mayer CE, Teh HY, Hafen K, Gallone G, Barthlott T, Ponting CP, Hollander GA, Foxn1 regulates key target genes essential for T cell development in postnatal thymic epithelial cells. Nat Immunol 17, 1206–1215 (2016). [PubMed: 27548434]
20. Nowell CS, Bredenkamp N, Tetelin S, Jin X, Tischner C, Vaidya H, Sheridan JM, Stenhouse FH, Heussen R, Smith AJ, Blackburn CC, Foxn1 regulates lineage progression in cortical and medullary thymic epithelial cells but is dispensable for medullary sublineage divergence. PLoS Genet 7, e1002348 (2011). [PubMed: 22072979]
21. Koch U, Fiorini E, Benedito R, Besseyrias V, Schuster-Gossler K, Pierres M, Manley NR, Duarte A, Macdonald HR, Radtke F, Delta-like 4 is the essential, nonredundant ligand for Notch1 during thymic T cell lineage commitment. J Exp Med 205, 2515–2523 (2008). [PubMed: 18824585]
22. Candi E, Rufini A, Terrinoni A, Giamboi-Miraglia A, Lena AM, Mantovani R, Knight R, Melino G, ΔNp63 regulates thymic development through enhanced expression of FgfR2 and Jag2. Proc Natl Acad Sci U S A 104, 11999–12004 (2007). [PubMed: 17626181]
23. Senoo M, Pinto F, Crum CP, McKeon F, p63 Is essential for the proliferative potential of stem cells in stratified epithelia. Cell 129, 523–536 (2007). [PubMed: 17482546]
24. Gordon J, Patel SR, Mishina Y, Manley NR, Evidence for an early role for BMP4 signaling in thymus and parathyroid morphogenesis. Dev Biol 339, 141–154 (2010). [PubMed: 20043899]
25. Tsai PT, Lee RA, Wu H, BMP4 acts upstream of FGF in modulating thymic stroma and regulating thymopoiesis. Blood 102, 3947–3953 (2003). [PubMed: 12920023]

26. Barsanti M, Lim JM, Hun ML, Lister N, Wong K, Hammett MV, Lepletier A, Boyd RL, Giudice A, Chidgey AP, A novel Foxn1$^{eGFP/+}$ mouse model identifies Bmp4-induced maintenance of *Foxn1* expression and thymic epithelial progenitor populations. Eur J Immunol 47, 291–304 (2017). [PubMed: 27861793]
27. Lepletier A, Hun ML, Hammett MV, Wong K, Naeem H, Hedger M, Loveland K, Chidgey AP, Interplay between Follistatin, Activin A, and BMP4 Signaling Regulates Postnatal Thymic Epithelial Progenitor Cell Differentiation during Aging. Cell Rep 27, 3887–3901 e3884 (2019). [PubMed: 31242421]
28. Zou D, Silvius D, Davenport J, Grifone R, Maire P, Xu PX, Patterning of the third pharyngeal pouch into thymus/parathyroid by Six and Eya1. Dev Biol 293, 499–512 (2006). [PubMed: 16530750]
29. Feng J, Jing J, Sanchez-Lara PA, Bootwalla MS, Buckley J, Wu N, Yan Y, Chai Y, Generation and characterization of tamoxifen-inducible Pax9-CreER knock-in mice using CrispR/Cas9. Genesis 54, 490–496 (2016). [PubMed: 27381449]
30. Wallin J, Eibel H, Neubuser A, Wilting J, Koseki H, Balling R, Pax1 is expressed during development of the thymus epithelium and is required for normal T-cell maturation. Development 122, 23–30 (1996). [PubMed: 8565834]
31. Peters H, Neubuser A, Kratochwil K, Balling R, *Pax9*-deficient mice lack pharyngeal pouch derivatives and teeth and exhibit craniofacial and limb abnormalities. Genes Dev 12, 2735–2747 (1998). [PubMed: 9732271]
32. Das P, Stockton DW, Bauer C, Shaffer LG, D'Souza RN, Wright T, Patel PI, Haploinsufficiency of *PAX9* is associated with autosomal dominant hypodontia. Hum Genet 110, 371–376 (2002). [PubMed: 11941488]
33. Frank J, Pignata C, Panteleyev AA, Prowse DM, Baden H, Weiner L, Gaetaniello L, Ahmad W, Pozzi N, Cserhalmi-Friedman PB, Aita VM, Uyttendaele H, Gordon D, Ott J, Brissette JL, Christiano AM, Exposing the human nude phenotype. Nature 398, 473–474 (1999). [PubMed: 10206641]
34. Nehls M, Pfeifer D, Schorpp M, Hedrich H, Boehm T, New member of the winged-helix protein family disrupted in mouse and rat nude mutations. Nature 372, 103–107 (1994). [PubMed: 7969402]
35. Bosticardo M, Yamazaki Y, Cowan J, Giardino G, Corsino C, Scalia G, Prencipe R, Ruffner M, Hill DA, Sakovich I, Yemialyanava I, Tam JS, Padem N, Elder ME, Sleasman JW, Perez E, Niebur H, Seroogy CM, Sharapova S, Gebbia J, Kleiner GI, Peake J, Abbott JK, Gelfand EW, Crestani E, Biggs C, Butte MJ, Hartog N, Hayward A, Chen K, Heimall J, Seeborg F, Bartnikas LM, Cooper MA, Pignata C, Bhandoola A, Notarangelo LD, Heterozygous *FOXN1* Variants Cause Low TRECs and Severe T Cell Lymphopenia, Revealing a Crucial Role of FOXN1 in Supporting Early Thymopoiesis. Am J Hum Genet 105, 549–561 (2019). [PubMed: 31447097]
36. Markert ML, Devlin BH, Alexieff MJ, Li J, McCarthy EA, Gupton SE, Chinn IK, Hale LP, Kepler TB, He M, Sarzotti M, Skinner MA, Rice HE, Hoehner JC, Review of 54 patients with complete DiGeorge anomaly enrolled in protocols for thymus transplantation: outcome of 44 consecutive transplants. Blood 109, 4539–4547 (2007). [PubMed: 17284531]
37. Markert ML, Marques JG, Neven B, Devlin BH, McCarthy EA, Chinn IK, Albuquerque AS, Silva SL, Pignata C, de Saint Basile G, Victorino RM, Picard C, Debre M, Mahlaoui N, Fischer A, Sousa AE, First use of thymus transplantation therapy for FOXN1 deficiency (nude/SCID): a report of 2 cases. Blood 117, 688–696 (2011). [PubMed: 20978268]
38. Davies EG, Cheung M, Gilmour K, Maimaris J, Curry J, Furmanski A, Sebire N, Halliday N, Mengrelis K, Adams S, Bernatoniene J, Bremner R, Browning M, Devlin B, Erichsen HC, Gaspar HB, Hutchison L, Ip W, Ifversen M, Leahy TR, McCarthy E, Moshous D, Neuling K, Pac M, Papadopol A, Parsley KL, Poliani L, Ricciardelli I, Sansom DM, Voor T, Worth A, Crompton T, Markert ML, Thrasher AJ, Thymus transplantation for complete DiGeorge syndrome: European experience. J Allergy Clin Immunol 140, 1660–1670 e1616 (2017). [PubMed: 28400115]
39. Janda A, Sedlacek P, Honig M, Friedrich W, Champagne M, Matsumoto T, Fischer A, Neven B, Contet A, Bensoussan D, Bordigoni P, Loeb D, Savage W, Jabado N, Bonilla FA, Slatter MA, Davies EG, Gennery AR, Multicenter survey on the outcome of transplantation of hematopoietic

cells in patients with the complete form of DiGeorge anomaly. Blood 116, 2229–2236 (2010). [PubMed: 20530285]

40. Feederle R, Gerber JK, Middleton A, Northrup E, Kist R, Kremmer E, Peters H, Generation of Pax1/PAX1-Specific Monoclonal Antibodies. Monoclon Antib Immunodiagn Immunother, (2016).
41. Ciancanelli MJ, Huang SX, Luthra P, Garner H, Itan Y, Volpi S, Lafaille FG, Trouillet C, Schmolke M, Albrecht RA, Israelsson E, Lim HK, Casadio M, Hermesh T, Lorenzo L, Leung LW, Pedergnana V, Boisson B, Okada S, Picard C, Ringuier B, Troussier F, Chaussabel D, Abel L, Pellier I, Notarangelo LD, Garcia-Sastre A, Basler CF, Geissmann F, Zhang SY, Snoeck HW, Casanova JL, Infectious disease. Life-threatening influenza and impaired interferon amplification in human IRF7 deficiency. Science 348, 448–453 (2015). [PubMed: 25814066]
42. Dobin A, Davis CA, Schlesinger F, Drenkow J, Zaleski C, Jha S, Batut P, Chaisson M, Gingeras TR, STAR: ultrafast universal RNA-seq aligner. Bioinformatics 29, 15–21 (2013). [PubMed: 23104886]
43. Harrow J, Frankish A, Gonzalez JM, Tapanari E, Diekhans M, Kokocinski F, Aken BL, Barrell D, Zadissa A, Searle S, Barnes I, Bignell A, Boychenko V, Hunt T, Kay M, Mukherjee G, Rajan J, Despacio-Reyes G, Saunders G, Steward C, Harte R, Lin M, Howald C, Tanzer A, Derrien T, Chrast J, Walters N, Balasubramanian S, Pei B, Tress M, Rodriguez JM, Ezkurdia I, van Baren J, Brent M, Haussler D, Kellis M, Valencia A, Reymond A, Gerstein M, Guigo R, Hubbard TJ, GENCODE: the reference human genome annotation for The ENCODE Project. Genome Res 22, 1760–1774 (2012). [PubMed: 22955987]
44. Liao Y, Smyth GK, Shi W, featureCounts: an efficient general purpose program for assigning sequence reads to genomic features. Bioinformatics 30, 923–930 (2014). [PubMed: 24227677]
45. Love MI, Huber W, Anders S, Moderated estimation of fold change and dispersion for RNA-seq data with DESeq2. Genome Biol 15, 550 (2014). [PubMed: 25516281]
46. R. C. Team, R: A language and environment for statistical computing. R Foundation for Statistical Computing, Vienna, Austria, (2014).
47. Benjamini Y, Hochberg Y, Controlling the False Discovery Rate - a Practical and Powerful Approach to Multiple Testing. J R Stat Soc B 57, 289–300 (1995).
48. Subramanian A, Tamayo P, Mootha VK, Mukherjee S, Ebert BL, Gillette MA, Paulovich A, Pomeroy SL, Golub TR, Lander ES, Mesirov JP, Gene set enrichment analysis: a knowledge-based approach for interpreting genome-wide expression profiles. Proc Natl Acad Sci U S A 102, 15545–15550 (2005). [PubMed: 16199517]

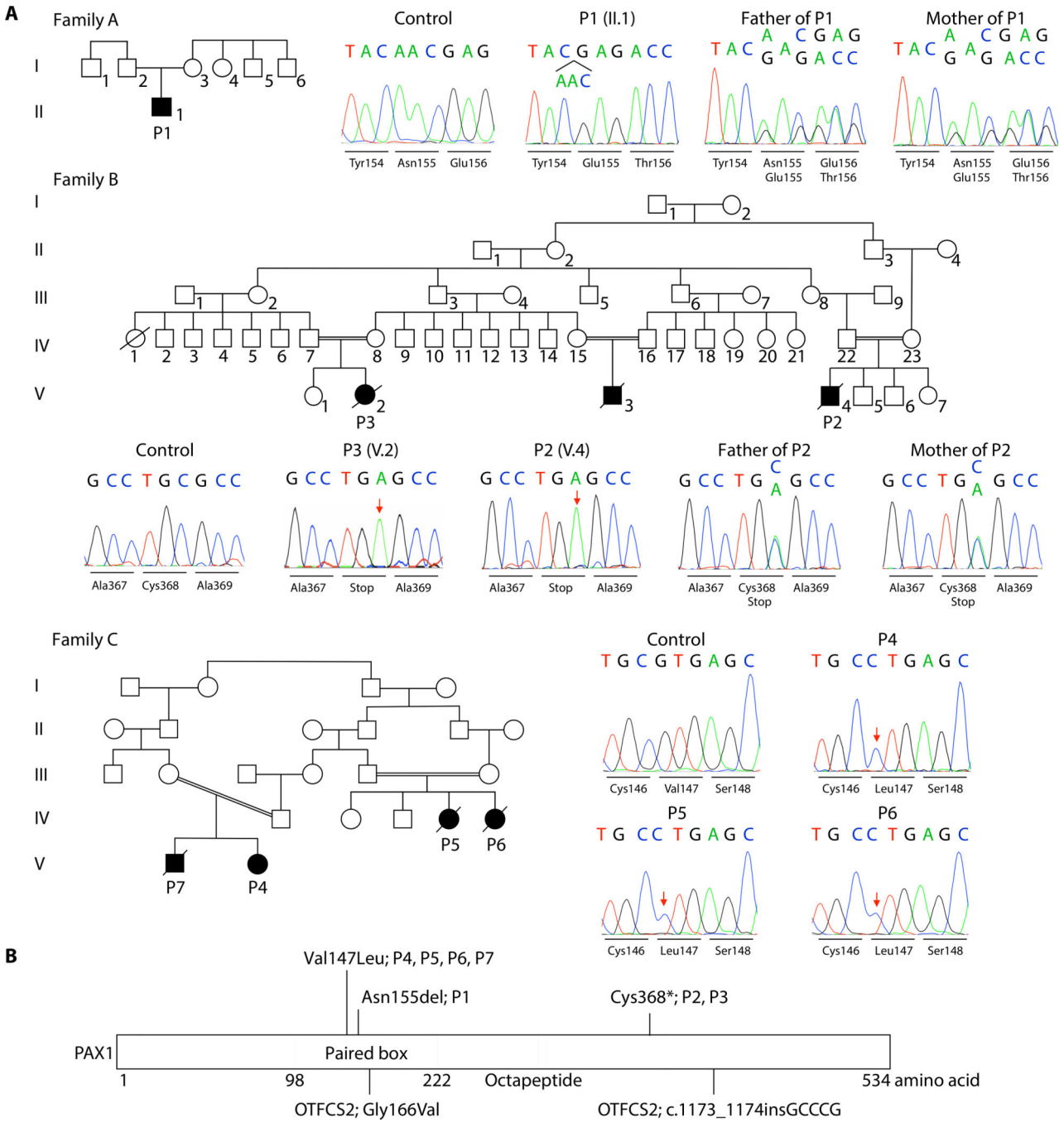

Fig. 1. Pedigrees and PAX1 genetic studies.

(A) Pedigrees and results of Sanger sequencing in patients with *PAX1* variants and in healthy controls. For both family A and family B, results of Sanger sequencing in the heterozygous parents are also shown.

(B) Schematic representation of the PAX1 protein, and location of the variants identified in affected individuals. OTFCS2: Otofaciocervical syndrome type 2.

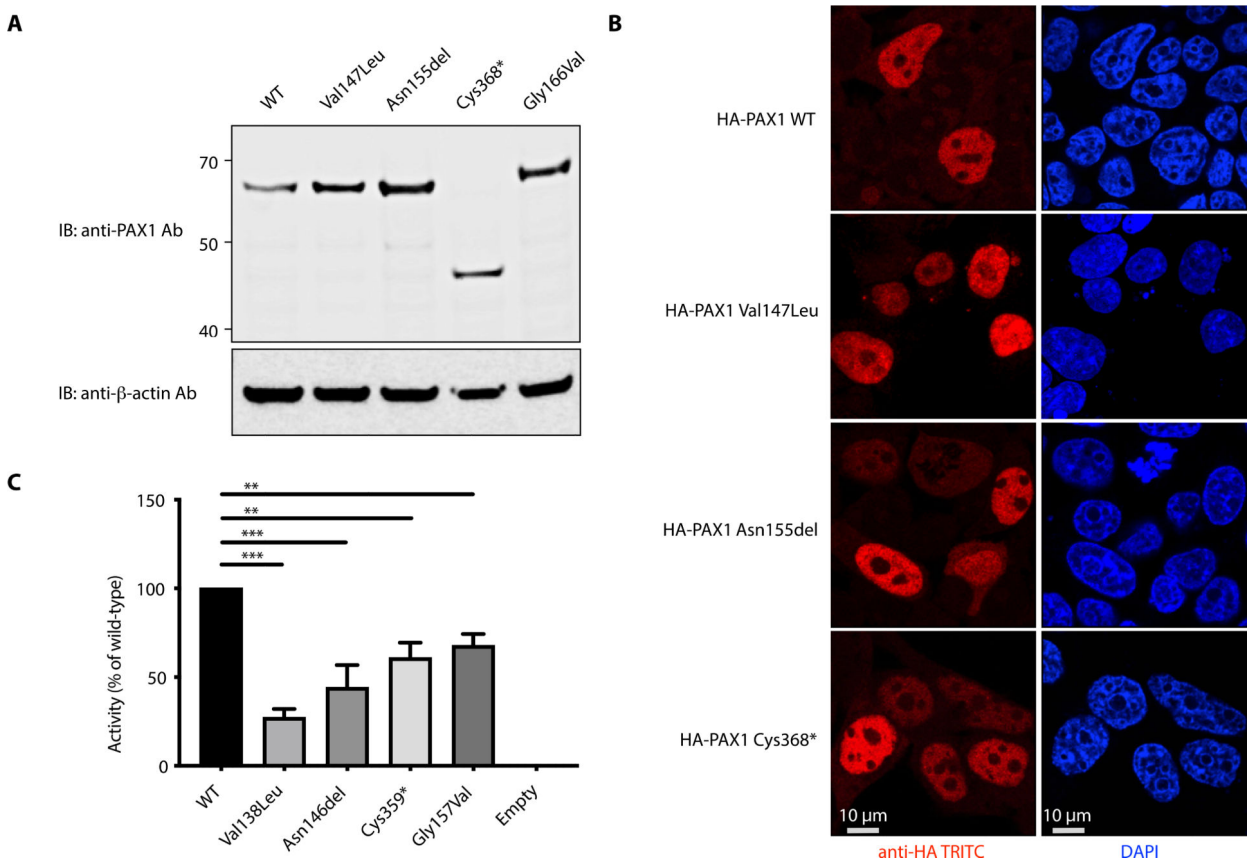

Fig. 2. Molecular and functional analysis of PAX1 mutant proteins.

(A) Western blot showing expression of wild-type and mutant human PAX1 proteins upon transient transfection in 293T cells.

(B) Left: Intracellular protein localization upon transfection of HA-tagged WT and mutant *PAX1* constructs into 293T cells, followed by staining with TRITC anti-HA. Right: counterstaining with DAPI, demonstrating that the mutant PAX1 protein retain nuclear translocation capacity. Scale bar indicates 10 μm.

(C) Results of a luciferase reporter assay demonstrating reduced transcriptional activity of mutant PAX1 proteins, corresponding to the PAX1 variants detected in patients. The promotor region of *Nkx3–2* was used to drive luciferase expression. Results of six independent experiments (each run in triplicate) are shown (mean ± SEM). P value was calculated with one-way ANOVA and adjusted by Dunnett's multiple comparisons test. **; $P<0.01$.

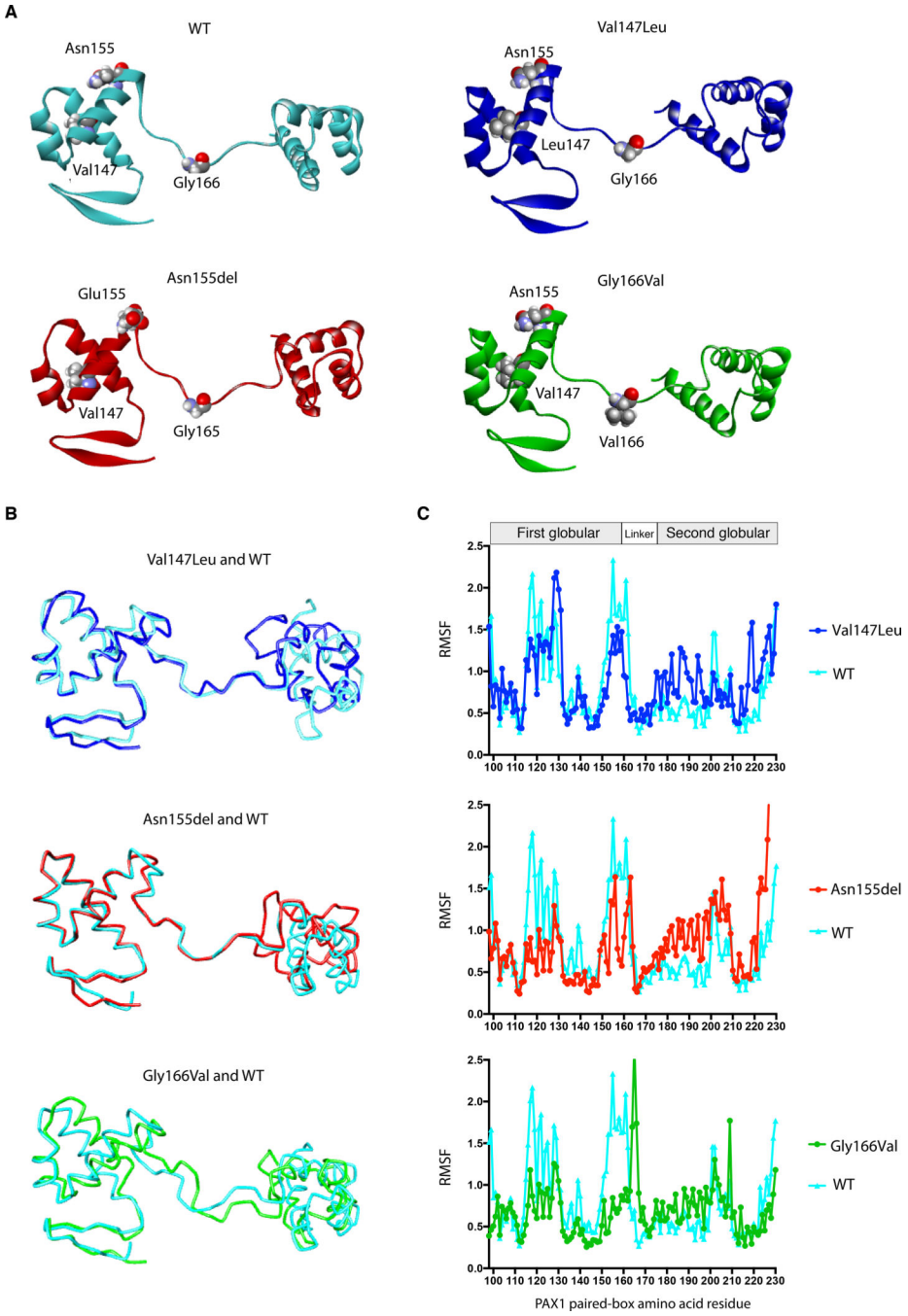

Fig. 3. In silico analysis of the PAX1 paired-box domain in WT and mutant proteins.

(A) Molecular modeling of the paired box domain of WT and mutant PAX1 proteins, showing presence of two globular domain separated by a linker. Note that the Asparagine residue at position 155 is adjacent to linker domain, and its deletion results in shortening of the last turn of the 3rd alpha helix in the first globular domain of the paired box domain. **(B)** Molecular superimposition of WT (in light blue) and mutant PAX1 variants after MD simulation, showing that the both the Val147Leu and the Asn155del variants predominantly

affect the conformation of the C-terminus globular domain, whereas both globular domains are affected by the Gly166Val variant.

(C) Root-mean-square fluctuation values (RMSF) of WT PAX1, and of the Val147Leu, Asn155del, and Gly166Val variants during MD simulations. RMSF are used here as a measure of the flexibility of different regions of the protein during the MD simulations. The Y-axes indicate the magnitude of the fluctuation while the X-axes indicate the specific location of each amino acid within the paired-box domain.

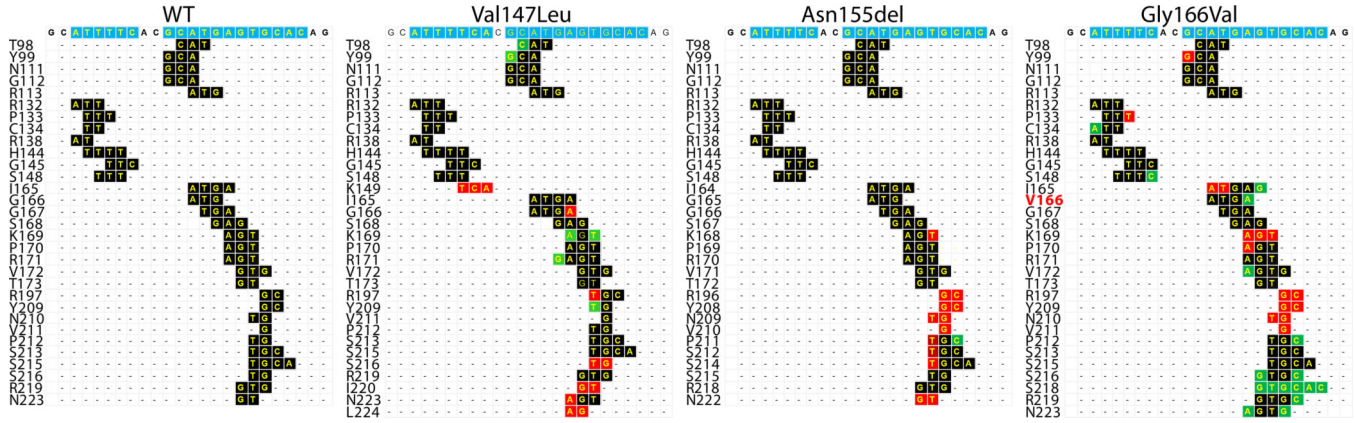

Fig. 4. Interface analysis of PAX1 paired-box domain and DNA interaction.

Shown in black are nucleotide residues with which the paired box domain of either WT or PAX1 mutant proteins establish interaction. The amino acids contacting nucleotides of target DNA are indicated on the Y-axis for each PAX1 protein. The red and green colors color indicate loss and gain of DNA binding, respectively.

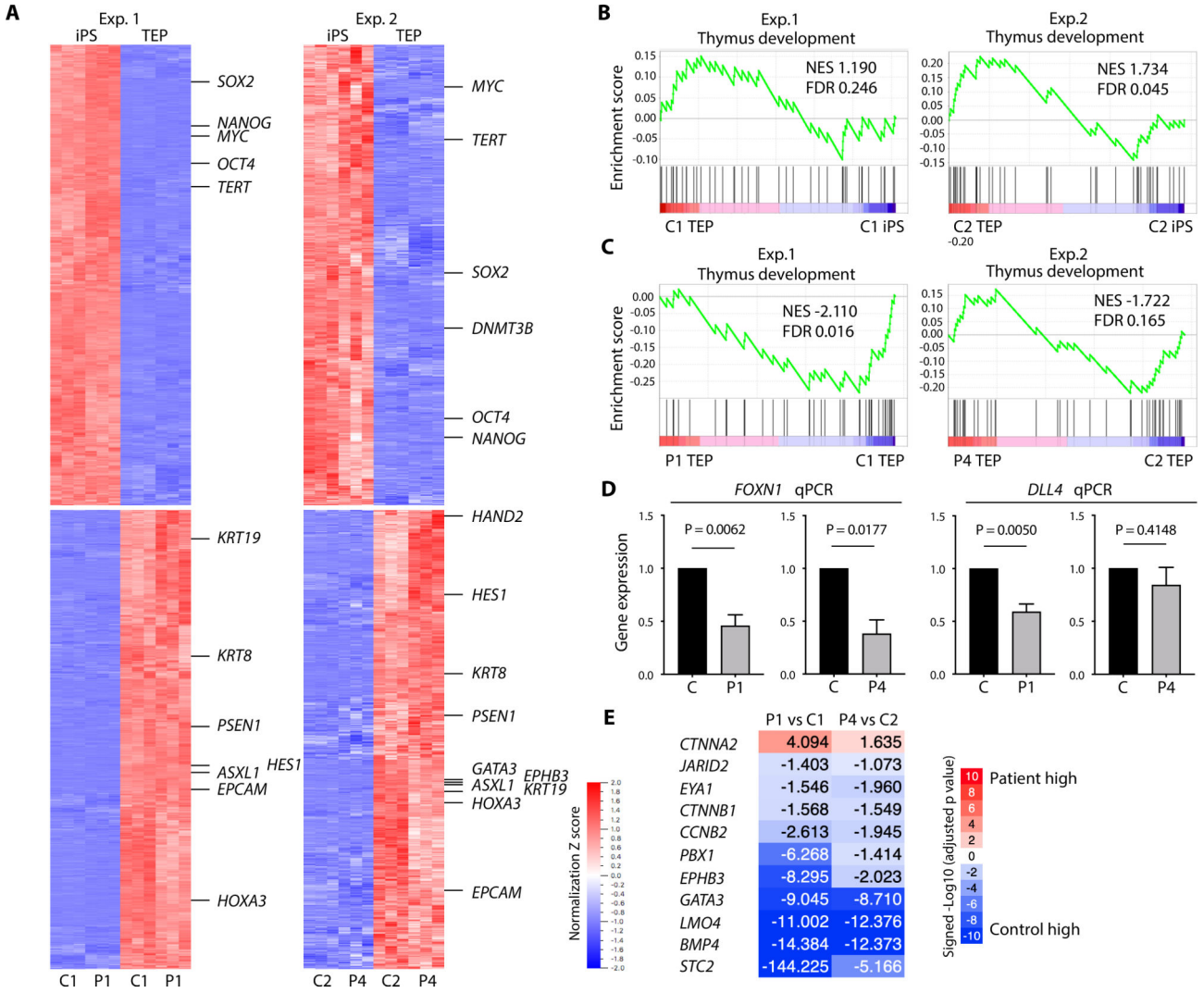

Fig. 5. Differentially expressed genes between control and patient TEPs

(A) Heatmap of differentially expressed genes between iPS and TEP stage as determined by RNA-seq. Each heatmap shows the top 3,000 genes which were differentially expressed between iPS and TEP cells, with a significance (q-value <0.01) by the 2-group comparison (t-test). Genes whose expression was found to be upregulated at the TEP stage included epithelial cell markers (*EPCAM, KRT8, KRT19*) as well as several genes (*PSEN1*, *HES1*, *ASXL1*, *HOXA3*, *HAND2*, *EPHB3*, *GATA3*) which appeared at the leading edge of GSEA of thymus development in panel B.

(B and C) GSEA on thymus development gene set by preranked genes according to -Signed log 10 adjusted p value. The adjusted p value was acquired by DEseq2 analysis using normalized read count of RNA seq data. (D) qRT-PCR analysis of *FOXN1* and *DLL4* expression at TEP stage of differentiation. Results are from five independent experiments for control and P1, and four independent experiments for control and P4, with triplicates in each case (mean ± SEM). The P value was calculated with two-tailed paired t-test. P<0.05 was considered to be significant. (E) Thymus development genes with evidence of differential expression between patient and control cells (adjusted p value <0.1 and concordant pattern

of expression in both RNA-seq experiments). For this comparison, we considered genes that were part of the “Thymus development” gene set in MSigDB v 7.0, and in the top 30 FOXN1-target genes reported by (19). The values displayed are the signed -log10 of the adjusted p value for differential expression.

Table 1 –

Laboratory data at presentation

Patient [age]	P1 [9 months]	P2 [14 days]	P3 [17 days]	P4 [1 month]	P5 [6 months]	P6 [1 month]	Control Values
ANC (cells $\times 10^{-3}/\mu L$)	0.52	2.77	6.36	1.22	3.8	3.96	1.0–9.0
ALC (cells $\times 10^{-3}/\mu L$)	2.09	2.18	2.46	2.34	46.7	1.55	3.4–7.6
AEoC (cells $\times 10^{-3}/\mu L$)	5.86	0.22	0.67	0.38	9.6	0.86	0.05–0.7
Platelets ($\times 10^{-9}/L$)	8	389	667	324	780	449	150–400
$CD3^+$ cells/μL	177	76	2	58	43985	18	2500–5500
$CD4^+$ cells/μL	103	87	0	50	10762	18	1600–4000
$CD8^+$ cells/μL	29	141	0	0	17313	0	560–1700
$CD19^+$ cells/μL	618	1482	1107	946	936	811	300–2000
$CD16/56^+$ cells/μL	208	359	1107	482	1404	1205	170–1100
In vitro proliferation to PHA (cpm $\times 10^{-3}$)	19.8 *	5.5	n.d.	2.16	2.5	0.65	[≥ 94.9]
IgG (mg/dL)	1450	745	658	690	170	650	611–1542
IgA (mg/dL)	27	<6.6	<6	<25	<25	<25	7–37
IgM (mg/dL)	21	25	17	49	117	<25	26–122
IgE (kU/L)	1241	730	<2	<2	10080	<2	0–9

* measured as % of $CD3^+$ cells incorporating Edu® (normal value: ≥58.5)

AEoC: Absolute Eosinophil Count; ALC: Absolute Lymphocyte Count); ANC: Absolute Neutrophil Count; n.d.: not done

Table 2 –

Hematopoietic Stem Cell Transplantation in Patients with Pathogenic *PAX1* Variants

Patient	**P1**	**P2**	**P3**	**P4**
Age at Transplantation	12 months	4.5 months	3.5 months	4 months
Transplant Characteristics				
Donor Type, HLA-matching	URD, 9/10	Mother, 4/8	Mother, 4/8	URD, 4/6
Source of Stem Cells	Bone Marrow	T-cell-depleted Bone Marrow	PBSC	Cord Blood
Conditioning Regimen	Alemtuzumab 1 mg/kg Fludarabine 150 mg/m^2 Melphalan 140 mg/m^2	Busulfan 8 mg/kg Cyclophosphamide 200 mg/kg	First HSCT: Treosulfan 30 g/m^2 Fludarabine 120 mg/m^2 ATG 4 mg/kg Second HSCT (7 months): Thiotepa 10 mg/kg Cyclophosphamide 150 mg/kg ATG 25 mg/kg	Busulfan 16 mg/kg Fludarabine 160 mg/m2 ATG 20 mg/kg
Engraftment and Immune Reconstitution				
Time post-transplant	9 months	2 months	11.5 months after 2nd HSCT	4 years
Chimerism (source)	100% Donor, Whole Blood	Autologous	78% Recipient; 22% Donor	100% Donor
ANC (×10^{-3}/μL)	1.96	4.5	3.27	2.99
ALC (×10^{-3}/μL)	0.71	0.45	2.7	0.44
CD3$^+$ cells/μL	247	9	54	24
CD4$^+$ cells/μL	76	4	13	21
CD8$^+$ cells/μL	128	13	0	4
CD19$^+$ cells/μL	189	36	2265	0 *
CD16/56$^+$ cells/μL	91	n.d.	323	86
Outcome, Age, Cause of Death	Alive, 6y 4m, waiting for thymic transplantation	Deceased, 9.5 m, Respiratory distress	Deceased, 4y 7m, septic shock	Alive, 4y 4m

* Post-rituximab for severe autoimmune hemolytic anemia.

ATG, Anti-Thymocyte Globulin; HCT, Hematopoietic Cell Transplantation; PBSC, Peripheral Blood Stem Cells; URD, Unrelated Donor